Earth and Planetary Science Letters 405 (2014) 98–109

Contents lists available at ScienceDirect

Earth and Planetary Science Letters

www.elsevier.com/locate/epsl

Electrical conductivity anisotropy in partially molten peridotite under shear deformation

Baohua Zhang [a,b,*], Takashi Yoshino [a], Daisuke Yamazaki [a], Geeth Manthilake [a], Tomoo Katsura [a]

[a] Institute for Study of the Earth's Interior, Okayama University, Misasa, Tottori-ken 682-0193, Japan
[b] Institute of Geochemistry, Chinese Academy of Sciences, Guiyang, Guizhou 550002, China

ARTICLE INFO

Article history:
Received 12 March 2014
Received in revised form 4 August 2014
Accepted 12 August 2014
Available online 14 September 2014
Editor: J. Brodholt

Keywords:
electrical conductivity
anisotropy
partial melt
peridotite
shear deformation

ABSTRACT

The electrical conductivity of partially molten peridotite was measured during deformation in simple shear at 1 GPa in a DIA type apparatus with a uniaxial deformation facility. To detect development of electrical anisotropy during deformation of partially molten system, the electrical conductivity was measured simultaneously in two directions of three principal axes: parallel and normal to the shear direction on the shear plane, and perpendicular to the shear plane. Impedance spectroscopy measurement was performed at temperatures of 1523 K for Fe-bearing and 1723 K for Fe-free samples, respectively, in a frequency range from 0.1 Hz to 1 MHz. The electrical conductivity of partially molten peridotite parallel to shear direction increased to more than one order of magnitude higher than those normal to shear direction on the shear plane. This conductivity difference is consistent with the magnitude of the conductivity anisotropy observed in the oceanic asthenosphere near the Eastern Pacific Rise. On the other hand, conductivity perpendicular to the shear plane decreased gradually after the initiation of shear and finally achieved a value close to that of olivine. The magnitude and development style of conductivity anisotropy was almost the same for both Fe-bearing and Fe-free melt-bearing systems, and also independent of shear strain. However, such conductivity anisotropy was not developed in melt-free samples during shear deformation, suggesting that the conductivity anisotropy requires a presence of partial melting under shear stress. Microstructural observations of deformed partially molten peridotite samples demonstrated that conductivity anisotropy was attributed to the elongation of melt pockets parallel to the shear direction. Horizontal electrical conductivity anisotropy revealed by magnetotelluric surveys in the oceanic asthenosphere can be well explained by the realignment of partial melt induced by shear stress.

© 2014 Elsevier B.V. All rights reserved.

1. Introduction

The lithosphere and asthenosphere are defined as the high velocity region at the top of the mantle and the lower velocity region under the lithosphere, respectively. These structures were considered to have been formed by heat loss by conductive heat transfer to the surface, and therefore, it was thought that the change from lithosphere to asthenosphere is rather gradual (McKenzie et al., 2005). However, recent seismological studies (Rychert et al., 2005; Kawakatsu et al., 2009; Schmer, 2012) have shown a sharp lithosphere–asthenosphere boundary (LAB). Therefore, we should reconsider the structure of the asthenosphere on the basis of independent evidence.

Ocean floor magnetotelluric (MT) investigations revealed a high-conductivity layer (HCL) with high anisotropy characterized by higher conductivity in the direction parallel to plate motion. This has been observed beneath the southern East Pacific Rise (Evans et al., 2005; Baba et al., 2006) and beneath the edge of the Cocos plate at the Middle America trench offshore of Nicaragua (Naif et al., 2013). To account anisotropic conductivity, two major hypotheses have been proposed, hydration of mantle minerals, especially olivine (Evans et al., 2005), and partial melting (Yoshino et al., 2006; Naif et al., 2013). Experimental studies on the conductivity of single crystal hydrous

* Corresponding author at: Institute for Study of the Earth's Interior, Okayama University, Misasa, Tottori-ken 682-0193, Japan. Tel.: +81 858 43 3758; fax: +81 858 43 2184.
E-mail addresses: zhangbh148@qq.com, zhangbaohua@vip.gyig.ac.cn (B. Zhang).

http://dx.doi.org/10.1016/j.epsl.2014.08.018
0012-821X/© 2014 Elsevier B.V. All rights reserved.

olivine (Yoshino et al., 2006; Poe et al., 2010; Yang, 2012) showed the small effect of water on electrical conductivity in olivine and the small magnitude of the conductivity anisotropy at high temperatures. In addition, the low storage capacity of water in olivine coexisting with peridotite mineral assemblage at depth of the oceanic asthenosphere is around 50 ppm owing to partitioning with other mantle phases (Hirschmann et al., 2009; Férot and Bolfan-Casanova, 2012). Such small amount of water in olivine cannot significantly raise conductivity of the oceanic asthenosphere (Yoshino and Katsura, 2013). Thus, it is clear now that proton conduction is insignificant for the oceanic asthenosphere. Therefore, the partial melting is the only reasonable hypothesis for the anisotropic HCL.

Previous experimental studies on the electrical properties of partially molten systems demonstrated that partial melting enhances bulk conductivity due to the much higher conductivity of the melt phase (Roberts and Tyburczy, 1999; ten Grotenhuis et al., 2005; Yoshino et al., 2010) and its high connectivity (Waff and Bulau, 1979; Faul et al., 1994; Yoshino et al., 2009). On the other hand, many laboratory deformation studies have shown that pronounced anisotropic redistribution of melt in partially molten rocks does occur during shear deformation (Holtzman et al., 2003a, 2003b; Kohlstedt and Holtzman, 2009). Therefore it is expected that the anisotropic melt distribution could cause the conductivity anisotropy.

Recently, Caricchi et al. (2011) measured reductions of electrical conductivity during deformation of melt-bearing olivine aggregates under torsion. However, in this study the electrical conductivity was determined in only one direction across the shear direction, and also the absolute values were much lower than that of the normal mantle. In addition, Caricchi et al.'s experimental setup produced large strain and stress gradients along the measurement direction. This complexity prevents us from directly applying their results to the oceanic asthenosphere. As a result, there are no experimental results showing the conductivity anisotropy of sheared partially molten peridotite to explain the geophysically observed anisotropic HCL.

In this paper we propose the hypothesis that melt pockets are elongated and aligned in the shear direction, causing conductivity anisotropy with higher conductivity in the direction normal to a mid-oceanic ridge (parallel to plate motion). To verify this partial melt hypothesis, we simultaneously measured conductivity parallel (x) and normal (y) to the shear direction on the shear plane, and perpendicular (z) to the shear plane in partially molten peridotite. Such experimental investigations are very important not only to elucidate the origin of the anisotropic HCL but also to figure out the cause of softening of the oceanic asthenosphere.

2. Experimental procedures

2.1. Sample synthesis

Two different (Fe-bearing and -free) types of partial molten peridotite samples were used to measure the electrical conductivity under shear deformation. The Fe-bearing peridotite samples were prepared by mixing powders of San Carlos olivine (88 vol.%), synthetic basaltic glass (2 vol.%), and natural chromite (10 vol.%). The basaltic glass with a typical composition of MORB was prepared from a mixture of SiO_2, TiO_2, Fe_2O_3, Al_2O_3, MgO, $CaCO_3$ and Na_2CO_3. The chromite was added to inhibit grain growth of olivine. The Fe-free peridotite samples were a mixture of forsterite (Mg_2SiO_4) (88 vol.%) and enstatite ($MgSiO_3$) (10 vol.%) with synthetic basalt (2 vol.%). The enstatite was used to suppress forsterite grain growth. Each constituent was prepared from a mixture of oxides (MgO, SiO_2 and Al_2O_3) and carbonates ($CaCO_3$ and Na_2CO_3). For Na and Ca-bearing basalt samples, oxide mixture was decarbonated in a furnace before the synthesis experiment. For the Fe-bearing sample, the oxide mixture was baked under Fe–FeO buffer to reduce ferric to ferrous iron. The Fe-bearing and -free partial molten peridotite samples were synthesized at a pressure of 1 GPa and temperatures of 1523 and 1723 K, respectively, for 2 h using a piston cylinder apparatus. The average grain size was about 6 μm for Fe-bearing sample and 11 μm for Fe-free sample, respectively. The chemical compositions of staring materials and run products are listed in Table 1.

2.2. In situ conductivity measurements under shear deformation

The partially molten peridotite samples (two volume percent melt) with homogeneously distributed melt were deformed in simple shear geometry at high temperatures and 1 GPa in a DIA-type apparatus that could perform uniaxial deformation. The widely used DIA-type apparatus with a deformation function is the D-DIA apparatus in which the differential rams in the upper and lower guide blocks advance the upper and lower anvils relatively to the horizontal anvils. However, the deformation function adopted in this apparatus is different from that of the D-DIA apparatus. The lower anvil has a hole to accommodate a differential tungsten carbide (WC) piston. Differential stresses are generated by movement of the differential piston, which are controlled by insertion of a wedge-shaped indenter (Fig. 1). Compared with the D-DIA apparatus, a distinguishing advantage of this apparatus is that a small WC piston embedded into the center of lower anvil can generate large displacements. The displacement rate of the inner small WC piston can be accurately controlled by measuring its positions with a laser.

A cell assembly for *in situ* electrical conductivity measurement under shear deformation is shown in Fig. 2. The assembly included a cubic pyrophyllite pressure medium with a 21-mm edge length, a ZrO_2 thermal insulator, and a cylindrical graphite furnace. The sliced rectangular sintered peridotite sample with a thickness of 0.4–0.8 mm was placed between two half-cylindrical forsterite single-crystal pistons (cut parallel to the forsterite b-axis) parallel to the compression axis. The two pistons plus the sample were surrounded by polycrystalline MgO and coated with a thin layer of hexagonal boron nitride (BN), which reduced the friction between the piston and MgO. To improve the grip between the sample and pistons, 5 μm deep grooves oriented in the shear normal direction were contrived on the surfaces of the sample and the piston. Three-dimensional conductivities of partially molten peridotite were measured in the directions parallel (x) and normal (y) to the shear direction on the shear plane, and perpendicular (z) to the shear plane (see Fig. 2b and c). Rhenium foils normal to the shear direction were placed as strain markers and also as electrodes for conductivity measurement in the shear direction. To maintain two independent electrical circuits during shear deformation, small size electrode was used for y or z directions.

The samples were compressed to a pressure of 1 GPa, heated to temperatures of 1523 K for Fe-bearing and 1723 K for Fe-free samples and then deformed by advancing the tungsten carbide piston with a constant displacement rate between 70 μm/h and 300 μm/h. After the desired pressure (1 GPa) was achieved, *in situ* conductivity measurement was conducted using a complex impedance analyzer (Solartron 1260 combined with Solartron 1296 interface). Once the conductivity was found to become stable at the desired temperature, the WC piston was advanced at a constant displacement rate for shear deformation. The conductivities of partially molten peridotite in x and y (or z) directions were measured every 20 min during shear deformation by impedance spectroscopy at frequencies of 0.1 Hz to 1 MHz. Representative impedance spectra of partially molten peridotite

Table 1
Chemical composition of Fe-bearing and Fe-free starting materials and run products.

Fe-bearing system							
Oxide	Olivine ($N=8$)	Chromite ($N=10$)	MORB ($N=15$)	PC55[a] ($N=12$)	A2522[b] ($N=9$)	A2528[b] ($N=10$)	A2535[b] ($N=7$)
SiO_2	39.81(0.47)	0.02(0.02)	50.72(0.41)	50.94(1.36)	51.33(1.37)	51.05(1.22)	49.75(1.03)
TiO_2		0.11(0.02)	0.55(0.04)	0.53(0.02)	0.52(0.03)	0.52(0.01)	0.14(0.06)
Al_2O_3	0.04(0.01)	56.95(1.16)	16.18(0.13)	20.18(0.54)	21.49(0.77)	20.63(0.62)	22.03(0.41)
Cr_2O_3		11.48(0.25)	0.01(0.01)	0.54(0.02)	0.86(0.11)	0.65(0.07)	0.64(0.11)
FeO	9.56(0.35)	11.08(0.14)	7.15(0.21)	7.23(0.26)	7.34(0.31)	7.28(0.29)	6.70(0.39)
MnO		0.09(0.03)	0.02(0.01)	0.01(0.01)	0.01(0.01)	0.01(0.01)	0.02(0.01)
MgO	50.34(1.34)	19.89(0.88)	10.69(0.13)	11.35(0.42)	12.65(0.46)	11.82(0.51)	12.11(1.23)
CaO	0.06(0.02)		12.45(0.26)	7.83(0.62)	3.33(0.26)	6.29(0.47)	6.09(0.96)
Na_2O		0.01(0.01)	1.77(0.07)	1.31(0.05)	0.90(0.03)	1.23(0.06)	0.51(0.09)
K_2O		0.02(0.01)	0.02(0.01)	0.01(0.01)	0.01(0.01)	0.01(0.01)	0.13(0.08)
Total	99.81	99.65	99.56	99.93	98.53	99.49	98.12
Fe-free system							
Oxide	Fo ($N=5$)	En ($N=6$)	Basalt ($N=10$)	PC341[a] ($N=7$)	A2484[b] ($N=9$)	A2502[b] ($N=10$)	A2510[b] ($N=7$)
SiO_2	43.21(0.92)	59.76(1.24)	50.94(0.61)	52.44(1.52)	61.20(2.15)	55.65(1.85)	54.12(0.98)
Al_2O_3	0.01(0.01)	0.01(0.02)	16.52(0.17)	15.26(0.77)	4.46(0.18)	11.73(0.54)	14.38(0.39)
MgO	56.98(1.14)	39.65(0.78)	22.84(1.46)	23.16(0.74)	27.52(1.26)	25.71(1.13)	24.33(1.29)
CaO	0.03(0.01)	0.10(0.03)	7.90(0.52)	6.42(0.25)	3.50(0.32)	4.27(0.32)	5.27(0.34)
Na_2O			1.10(0.05)	1.11(0.04)	0.90(0.03)	0.98(0.05)	1.03(0.03)
K_2O			0.02(0.01)	0.07(0.04)	0.07(0.02)	0.05(0.03)	0.02(0.02)
Total	100.23	99.52	99.32	98.46	97.65	98.39	99.15

Notes: Wt% oxides in starting materials. Olivine is San Carlos olivine; Chromite is from Dabie area, China; MORB glass was synthesized at 1523 K. Fo is Mg_2SiO_4 forsterite; En is $MgSiO_3$ enstatite; Basalt is Fe-free basalt that was synthesized at 1723 K. N denotes numbers of analysis and numbers in parentheses are 1σ deviation from the mean.
[a] Before deformation.
[b] After deformation.

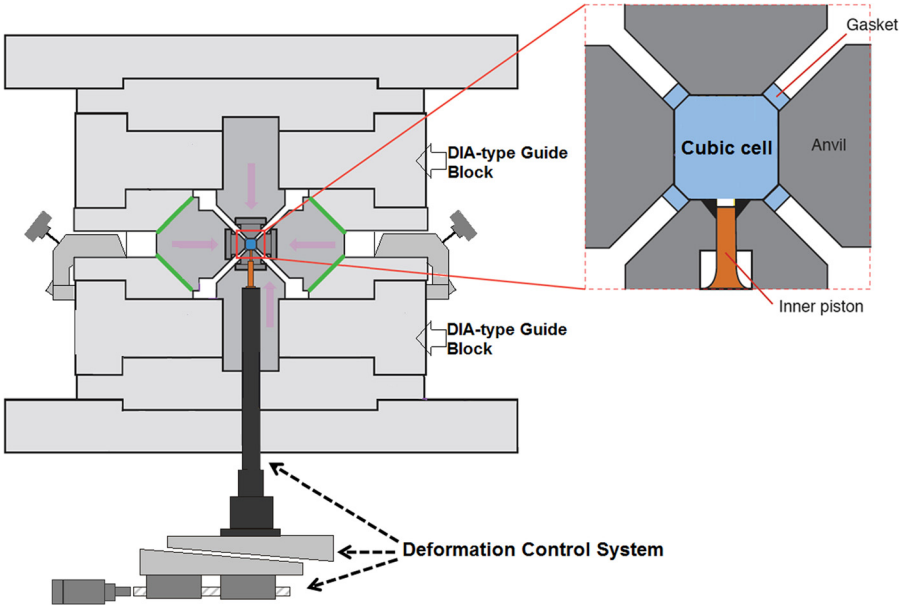

Fig. 1. Schematic drawing of the deformation DIA apparatus.

show one arc at high frequencies and an additional part appears at low frequencies (Fig. 3), which is a typical shape for spectra in partially molten systems (ten Grotenhuis et al., 2005; Yoshino et al., 2010). During the shear deformation, the radius of the impedance arc obtained from x direction decreases with increasing time (Fig. 3a). In contrast, the radius of the impedance arc normal to shear (y) direction remains almost constant throughout the experimental run (Fig. 3b). These observations implied that the electrical anisotropy was developed parallel to the shear direction during deformation of partially molten system.

A WRe_3–WRe_{25} thermocouple was set as an independent circuit insulated from the heater and the lead wires for the conductivity measurement. Unfortunately, this thermocouple was broken in most runs. Before the conductivity runs were made, the relationships between applied power and temperature were determined to control temperatures by power (Fig. 4). Because the heater was shortened by advancement of the piston, use of the constant power would result in slight increase of temperature (about 20∼30 K). In one run, the power was gradually decreased during shear deformation to keep the sample at constant temperature (Fig. 4b).

To determine the upper and lower bounds of conductivity of the Fe-free partially molten peridotite, the conductivities of Fe-free basalt melt and forsterite aggregate were also measured at temperatures up to 1873 K and a pressure of 1 GPa under static condition. The conductivity values of each phase at 1723 K and 1 GPa were

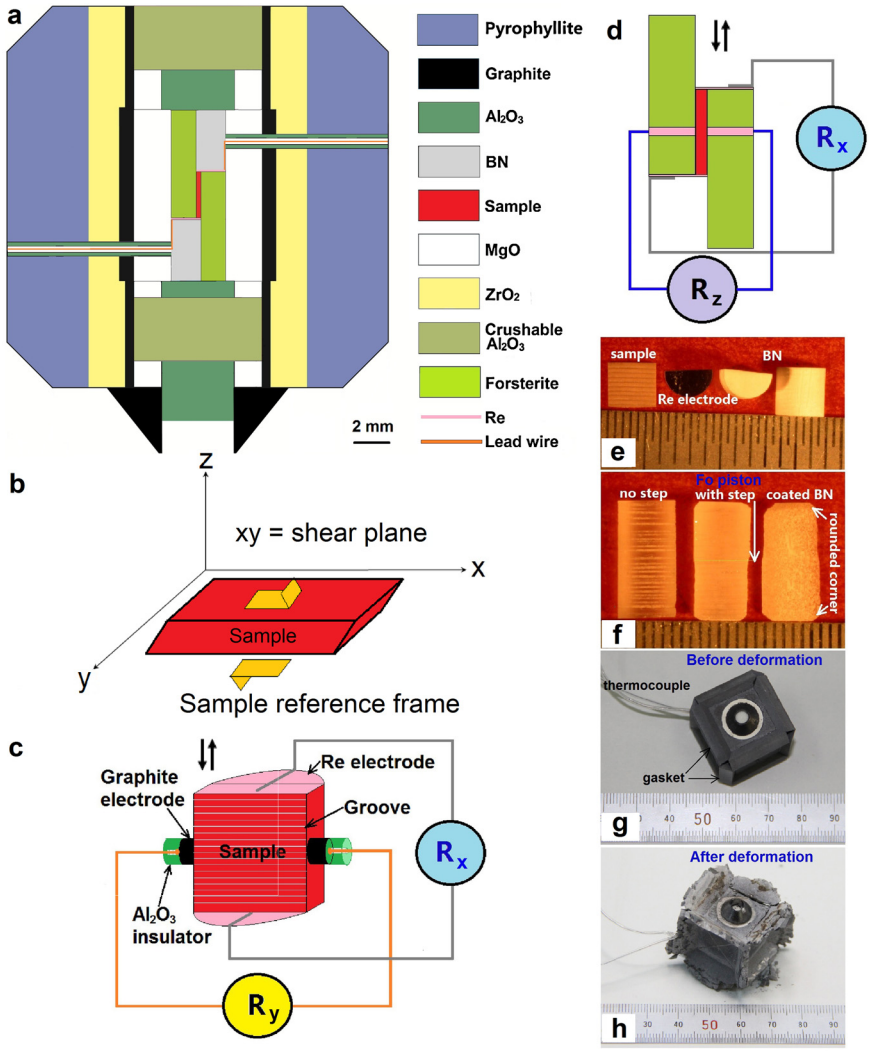

Fig. 2. Schematic drawing of cell assembly for shear deformation experiments. (a) Schematic cross-section of sample assembly for conductivity measurements under simple shear deformation (perpendicular to the shear plane). (b) 3D drawing of the slab sample showing three principle directions with respect to shear deformation. (c) Enlarged sketch of the sample, four electrode wires are shown in two directions (parallel (x) and normal (y) to shear direction) on the shear plane. (d) Conductivity measurement in the direction parallel to the shear direction (x) and normal to the shear plane (z). (e)–(h) Photos of the parts of the assembly.

$10^{1.1}$ and $10^{-2.7}$ (S/m), respectively. The experimental conditions are summarized in Table 2.

2.3. Microstructural analysis

To characterize the alignment and distribution of the melt phase in olivine-rich matrix quantitatively, we performed image analysis on back-scattered electron (BSE) images from two different polished sections cut parallel (xz plane) and normal (yz plane) to the shear direction for each deformed sample. The least fractured areas were selected for imaging at higher magnification. For the Fe-free samples, a sharp contrast image allowed a separation of melt and solid phases by a threshold method of image processing. However, for Fe-bearing samples, a direct threshold method of image processing was not applicable, because the olivine and pyroxene crystals had iron-rich rims that grew from the melt during quenching (Yoshino et al., 2005). These parts were manually regarded as melt in the image analysis. The long axis of melt pockets was obtained by elliptical approximation. The area of each region was determined by counting the number of pixels it occupied.

In addition, image analyses were performed to characterize variation of the melt fraction across the sheared sample. The analyzed area covered nearly half of the polished surface of the sample. The amount of melt was measured each bin rectangular with 4 μm interval parallel to the shear direction across the shear plane. These data were converted into the frequency distribution of melt fraction along the z direction.

3. Results

3.1. Effect of deformation on the electrical conductivity in partially molten peridotite

Fig. 5 shows the results of the conductivity measurements for melt-bearing and melt-free peridotite as a function of time. The melt-bearing peridotite had higher electrical conductivity than the melt-free peridotite from the beginning, suggesting that the melt in the olivine-rich matrix was interconnected. The actual conductivity value for the Fe-bearing sample was lower by a half order of magnitude than that for the Fe-free sample, because the measurement temperature of the Fe-bearing sample was lower than that of the Fe-free sample. As electric charges are transferred by body motion of ions in a melt, the presence of Fe ions had only a small effect on the melt conductivity. Conductivity of the partially molten peridotite parallel to the shear direction was initially identical to that normal to the shear direction. However, shear-

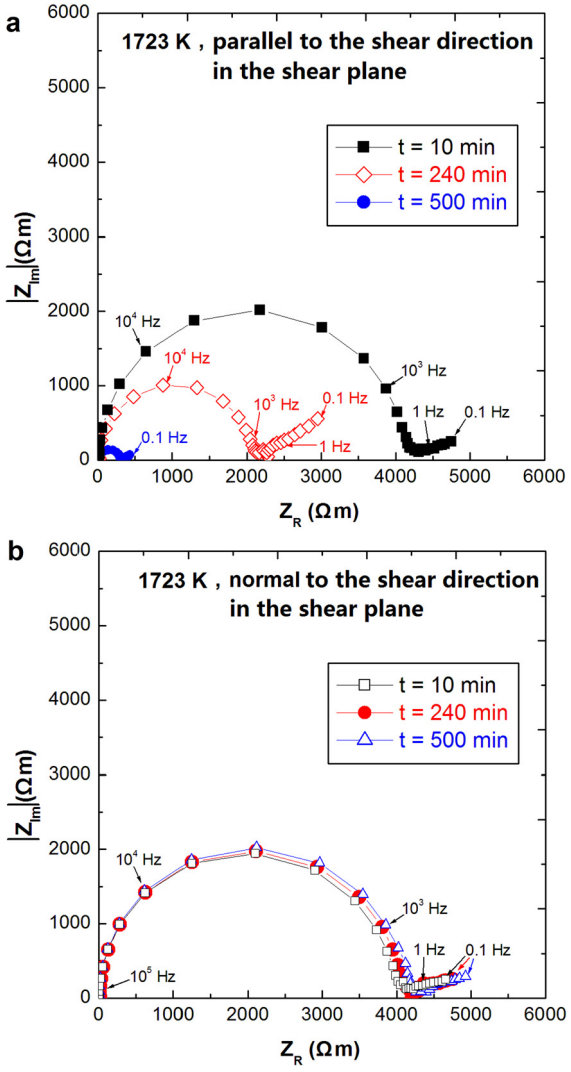

Fig. 3. Representative impedance spectra of the deformed partially molten peridotite (run A2502) at 10, 240 and 500 min after onset of the advancement of the piston. (a) Parallel and (b) normal to the shear direction in the shear plane.

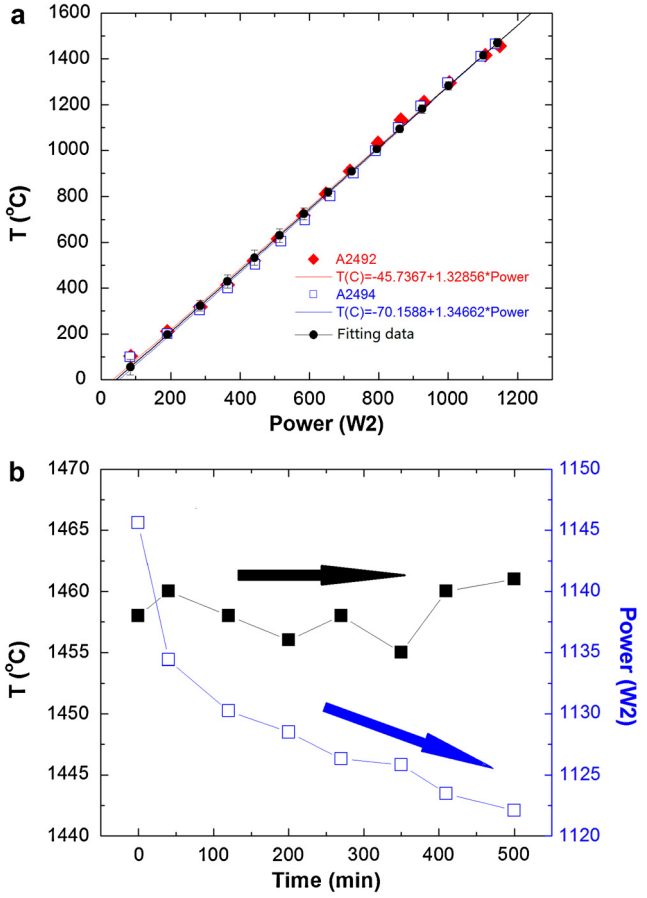

Fig. 4. Relationship between temperature and power during heating. (a) Increasing temperature to the desired value. (b) Maintaining at a constant temperature (1723 K) during shear deformation.

parallel (x) conductivity increased by more than one order of magnitude after the initiation of shear by piston advancement, and then remained constant for the duration of the experimental run. Conversely, y-direction conductivity remained constant, whereas z-direction conductivity decreased gradually after the initiation of shear and finally achieved a value close to that of olivine (Fig. 5a). As a result, the difference between shear-parallel (x) and shear-normal (y) conductivity reached one order of magnitude, and the

Table 2
Summary of experimental conditions.

Run No.	T (K)	ϕ^{d}	ϕ^{e}	G (μm)	d (mm)	L (μm)	υ (μm/h)	t (min)	γ	$\dot{\gamma}$ (s^{-1})	$\Delta(\log\sigma)^{f}$	Remarks[g]
A2522[a]	1523	0.019	0.025	8	0.42	680	100	490	1.73	5.88×10^{-5}	1.00	Const. P
A2528[a]	1523	0.019	0.023	10	0.80	585	70	600	0.24	6.67×10^{-6}	0.95	Decrease P
A2535[a]	1523	0.019	0.021	9	0.70	646	70	570	0.65	1.90×10^{-5}	1.46[h]	Decrease P
A2484[b]	1723	0.022	0.030	20	0.66	1200	100	660	0.36	9.09×10^{-6}	1.12	Const. P
A2502[b]	1723	0.022	0.026	18	0.58	745	100	500	1.0	3.33×10^{-5}	1.14	Decrease P
A2510[b]	1723	0.022	0.024	15	0.55	920	200	390	1.6	6.84×10^{-5}	1.08	TC control
A2506[c]	1723	0	0	12	0.52	1100	300	400	1.2	5.0×10^{-5}	~0	Const. P
A2509[c]	1723	0	0	17	0.58	1330	80	950	1.8	3.16×10^{-5}	~0	TC control

Notes: All experiments were conducted at 1 GPa.
Abbreviations: ϕ, melt fraction; G, average grain size; d, sample thickness; L, displacement; υ, displacement rate of the differential piston; t, duration; γ, final shear strain; $\dot{\gamma}$, shear strain rate.
[a] Ol + Chr + MORB.
[b] Fo + En + Ba.
[c] Fo aggregate.
[d] Before shear deformation.
[e] After shear deformation.
[f] Conductivity anisotropy is defined as $\Delta(\log\sigma) = \log\sigma_x - \log\sigma_y$.
[g] Method to maintain constant temperature. Const. P: constant power; Decrease P: slightly decreased power during deformation; TC control: thermocouple control.
[h] In Run A2535, $\Delta(\log\sigma) = \log\sigma_x - \log\sigma_z$.

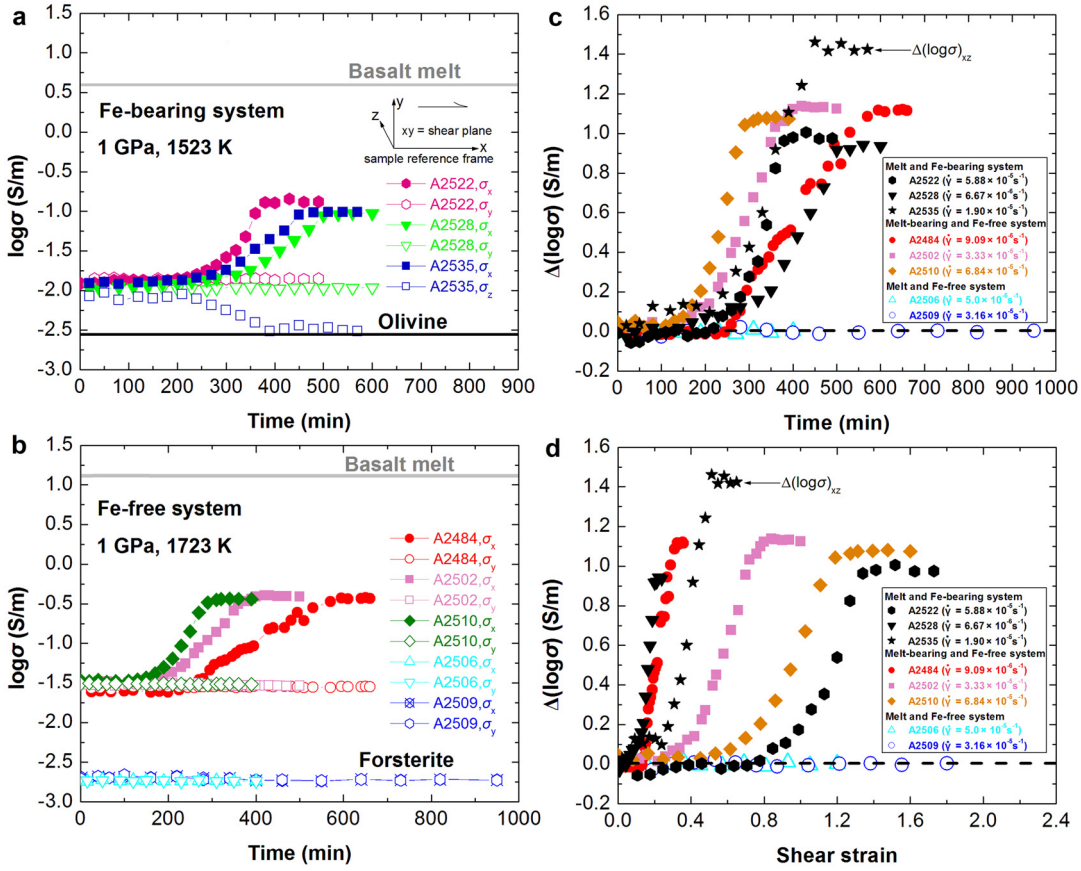

Fig. 5. Electrical conductivity of partially molten peridotites parallel and normal to the shear direction as functions of time and shear strain under shear deformation. (a) Fe-bearing system at 1523 K. The conductivities of Fe-bearing basaltic melt ($10^{0.6}$ S/m) (Presnall et al., 1972) and olivine ($10^{-2.54}$ S/m) (Constable, 2006) are also shown. (b) Fe-free system at 1723 K. Note that the conductivity values parallel (x) to the shear direction increase with increasing time for shear deformation, whereas those normal (y) to the shear direction are almost constant. For Run A2535 in a, the conductivity values perpendicular (z) to the shear plane gradually decrease with increasing time. Conductivity anisotropy [$\Delta(\log\sigma)$] of samples under shear deformation as a function of time (c) and shear strain (d). $\Delta(\log\sigma)$ is defined as the difference between logarithmic conductivity parallel (x) and normal (y) to the shear direction in the shear plane. The $\Delta(\log\sigma)$ of melt-bearing samples increases with time and strain, whereas that of melt-free samples remains zero. At its peak and when the conductivity stops changing, the conductivity parallel to the shear direction is one order of magnitude higher than that normal to the shear direction. $\dot{\gamma}$ is shear strain rate. Note that $\Delta(\log\sigma)$ in Run A2535 (★) is the difference between logarithmic conductivity parallel (x) to the shear direction in the shear plane and normal to the shear direction perpendicular (z) to the shear plane as mentioned in Table 2.

difference between shear-parallel (x) conductivity and that perpendicular (z) to the shear plane was 1.5 orders of magnitude.

On the other hand, such electrical conductivity anisotropy was not observed in melt-free samples (Fig. 5b), suggesting that the conductivity anisotropy is produced by partial melting under shear stress. The conductivities of partially molten peridotite were reasonably located between the upper (melt) and lower (olivine) bounds. Furthermore, the development of conductivity anisotropy started the nearly same duration (~200 min after the onset of piston advancement) (Fig. 5c), whereas it did not occur at similar shear strain (Fig. 5d). These observations suggest that shear strain has little effect on the conductivity anisotropy during shear deformation. Thus the conductivity anisotropy should not be caused by creep of grains, but by kinetics of melt migration under shear stress. Note that the magnitude and development style of conductivity anisotropy was almost the same for both Fe-bearing and Fe-free melt-bearing systems.

3.2. *Microstructure and melt composition before and after shear deformation*

Fig. 6 shows BSE images of the starting material and their image analysis results. For the Fe-bearing system, melt distribution was homogeneous, and rounded chromite grains at the triple junction of olivine crystals were surrounded by partial melt. In the Fe-free starting material, most melt was located at triple junctions composed of three olivine crystals, whereas melt was rare in the enstatite-rich area. Preferential melt distribution around olivine crystal was most probably caused by different wetting properties of olivine and orthopyroxene grains against basaltic melt (Toramaru and Fujii, 1986). Nevertheless, overall melt distribution was homogeneous and has no shape preferred orientation.

The microstructures of the deformed partially molten peridotite samples were examined from optical and BSE images. In each system, samples were deformed to several different finite strains. Shear deformation creates a marked anisotropy in melt distribution, as melt redistributes from randomly oriented melt-filled pockets into pockets with a strong preferred orientation (MPO). Finally melt segregation occurs beyond the grain scale. Fig. 7 shows the optical and BSE images from the polished section parallel to the shear direction (xz plane). The forsterite single-crystal pistons did not change its shape. Melt pockets preferentially occupied grain boundaries parallel to the shear direction and were elongated in the shear direction (Fig. 7e). Melt seems to segregate from an initial homogeneous distribution into two melt-rich regions parallel to the shear direction, separated by one melt-depleted region. As a result, the variation of melt fraction across the shear plane shows two peaks in Fig. 7d. The localizations of these two melt-rich layers are close to the upper and lower sample-piston boundaries.

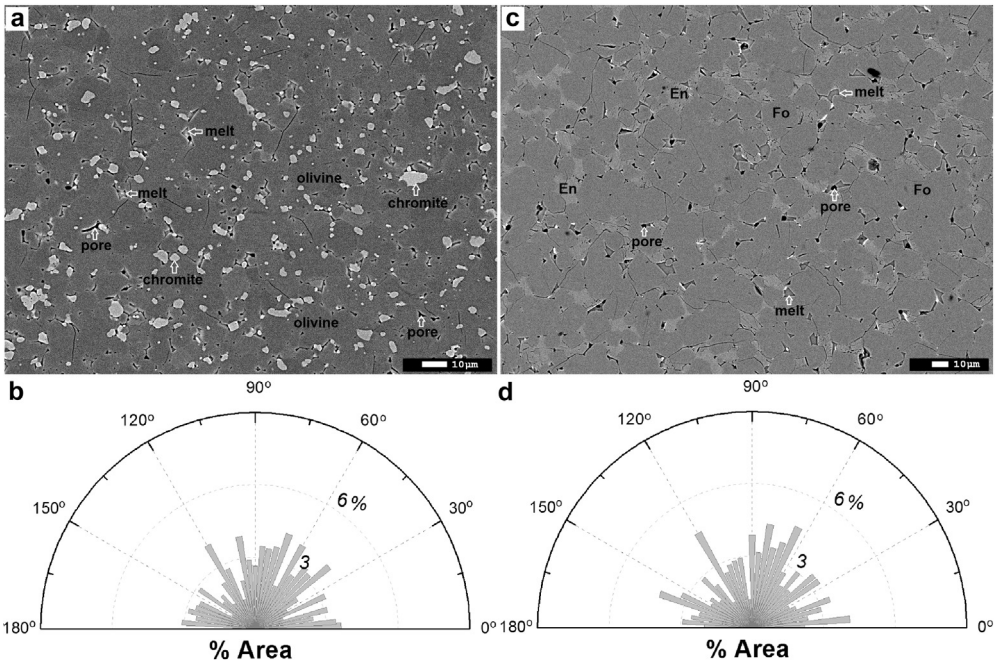

Fig. 6. Microstructure and melt distribution of starting material after heating to 1523 (Fe-bearing) and 1723 K (Fe-free) at 1 GPa but with no shear deformation. (a) Back-scattered electron image (BSE) of a sample (PC55) of the Fe-bearing partially molten sample. (b) The melt area weighted orientation defined by the long axis of melt pockets (MPO), which is plotted as a percentage of the total melt area. En = enstatite, Fo = forsterite. (c) BSE image of a starting sample (PC341) of the Fe-free system. (d) MPO of the Fe-free starting material is plotted as percent area. Over 750 individual melt pockets were measured for each graph in (b) and (d).

In contrast to the *xz* plane parallel to the shear direction, the melt pockets on the *yz* plane were characterized by a small cross-sectional area and isolated distribution. Thus, the three-dimensional morphology of an individual melt pocket has a tube-like geometry that is elongated parallel to the shear direction. These observations suggest that the development of conductivity anisotropy was caused by the realignment of partial melt to form a mesh of tube-like melt oriented in the shear direction.

After shear deformation, average grain size was slightly larger than that before shear deformation experiment (less than factor of 2). Melt fraction determined from large area including melt-rich and melt-less parts was slightly higher that of the starting material (Table 2). Although chemical composition of partial melt cannot be well constrained by EPMA analysis due to its small area, it seems to be changed in the Fe-free system, whereas melt composition of the Fe-bearing sample did not change significantly (Table 1). Although the slight change of chemical composition of melt was probably caused by a systematic temperature change in the cell during shear deformation, the total melt fraction including both melt-free and -bearing parts did not change largely before and after shear deformation. Therefore, the change of conductivity values during shear deformation is mostly attributed to the melt redistribution.

4. Discussion

4.1. Melt topology

The present study demonstrates development of the conductivity anisotropy during shear deformation. To estimate the interconnection of basaltic melt in the silicate matrix for each direction, the present results were compared with possible conduction models for a material. Fig. 8 shows conductivity–melt fraction relation for various effective media models. Details of the effective media models are given by Xu et al. (2000). Before the shear deformation, the conductivity values are a bit lower than those calculated from the Hashin–Shtrikman upper bound (HS^+), cube and tube-models, which assume interconnection of melt channel along the grain edges or grain boundaries. It is probably caused by a presence of secondary phase with wetting properties worse than olivine (Toramaru and Fujii, 1986). After the development of conductivity anisotropy, the conductivity values for the *x* direction are close to those predicted form parallel model and higher than the HS^+, suggesting that the melt linearly interconnects without tortuosity. In contrast, the *z* direction conductivity value is too low to explain all models considering interconnection and is close to that estimated from the series model, corresponding to the no interconnection of conductive phase between two electrodes.

The present study also demonstrates that two melt-rich domains presented in the *xz* plane were separated by one melt-depleted domain. The melt separation is caused by the gradient in applied stress in partially molten sample during shear deformation (Holtzman et al., 2003b; Kohlstedt and Holtzman, 2009). When stress induces alignment of melt pockets along the shear direction by small stress fluctuation, the permeability becomes anisotropic which significantly influences the transport properties of partially molten system. Once the melt pockets form, the mean stress in the melt-rich region is lower than the mean stress in the melt-poor region. The melt-rich channel will most effectively partition strain and induce the melt accumulation along the shear direction. The resulting viscosity of partially molten sample also enhances anisotropic deformation along the tube-like melt channel because major part of the total strain is accommodated on the relatively weak melt-rich region.

It is found that the melt distributions observed in this study are distinctly different from those in partially molten rocks reported in the previous works (e.g., Holtzman et al., 2003a, 2003b; Holtzman and Kohlstedt, 2007; Kohlstedt and Holtzman, 2009; Soustelle et al., 2014). Most previous experiments indicate that melt segregates into distinct melt-rich bands oriented ~20° antithetic to the macroscopic shear plane during samples were sheared, whereas melt-rich layers aligned parallel (~0°) to the shear direction in this study. This discrepancy is probably caused by different geometry for deformation experiments. The cylindrical piston cut at an angle

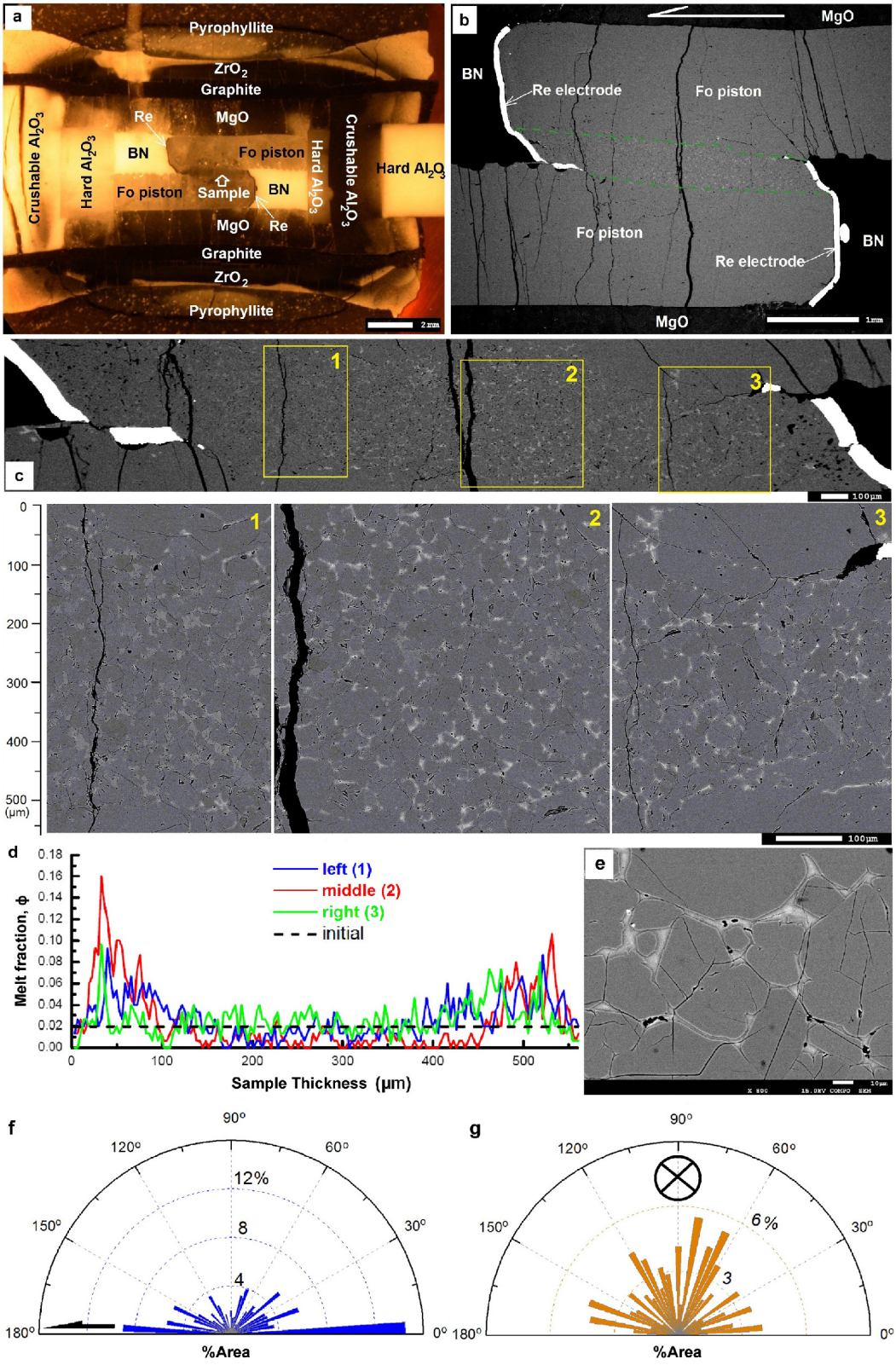

Fig. 7. Optical and back-scattered electron images of Fe-free partially molten sample (A2502) with $\phi = 0.02$ melt, deformed to 100% shear strain. (a) Overview optical image of the shear deformed sample between two forsterite single-crystal pistons on the polished section, which is parallel to the shear direction and normal to the shear plane. The grooves on the forsterite piston can be seen at contact with BN. (b) BSE image of the polished section in the same orientation as (a), at a higher magnification. Note that the Re electrodes were inclined by shear deformation. The dashed green lines indicate the boundary between the sample and forsterite piston. (c) Whole sample image. Numbers and yellow boxes indicate the magnified portions. (d) Melt distribution as a function of the sample thickness. Note that two peaks appear at the upper and lower boundary, which suggested that melt segregation occurred and formed two melt-rich regions parallel to the shear direction, separated by one melt-depleted region. (e) Higher magnification BSE image shows that melt pockets were preferentially occupied grain boundaries and were elongated in the shear direction. (f) Orientation of the long axis of melt pockets (MPO) as a percentage of the total melt area when viewed in a section cut parallel to the shear direction. (g) MPO as percentage of area in a section cut normal to the shear direction. (For interpretation of the references to color in this figure legend, the reader is referred to the web version of this article.)

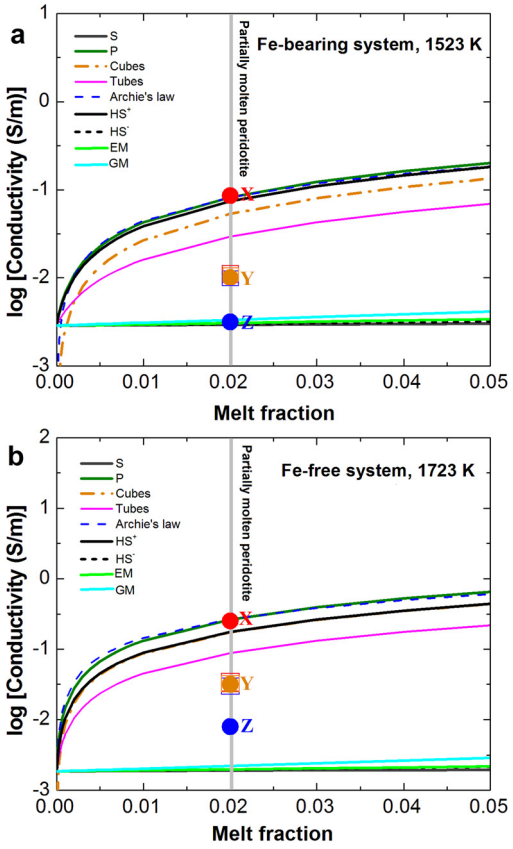

Fig. 8. Logarithm of electrical conductivity versus melt fraction for Fe-bearing (a) and Fe-free (b) systems. Lines indicate several effective media models for conductivity of the two-phase mixture. Square symbols denote the conductivity values before shear deformation. Close circle indicates the conductivity values after development of shear deformation (X, Y, Z denote the three directions for conductivity measurements). Abbreviations: S, series model; P, parallel model; HS^+, Hashin–Shtrikman upper bound; HS^-, Hashin–Shtrikman lower bound (Hashin and Shtrikman, 1962); EM, effective medium theory (Landauer, 1952); and GM, geometrical mean model (Shankland and Duba, 1990).

of 90° in this study, whereas the cut angle was 45° in most previous studies. As a result, nearly simple shear was applied for our deformed samples. However, the conventionally used 45° cut piston should provide not only simple shear component but also pure shear one in the deformed samples. For example, Holtzman et al. (2003a) observed decrease in sample thickness by up to 20% with increasing strain, accommodated by non-coaxial deformation. Our deformed samples did not show such large shortening. Because for the 45° cut geometry the minimum principle stress (σ_3) direction does not match the shear plane, the melt-rich bands oriented ~20° from the shear plane. However, for the 90° cut geometry in this study, it is expected to form two melt-rich regions parallel to the shear direction owing to the rotation of the maximum principle stress (σ_1) direction.

4.2. Origin of melt realignment

The strain rates in the present experiment were around $10^{-5}s^{-1}$ whereas the expected strain rates in the asthenosphere were 10^{-12}–10^{-14} s^{-1} (Kohlstedt and Holtzman, 2009). Thus, the stresses (or strain rates) in our experiments were considerably higher than those predicted in the asthenosphere. Experimental (Holtzman et al., 2003a, 2003b; Holtzman and Kohlstedt, 2007; Kohlstedt and Holtzman, 2009) and theoretical (Hier-Majumder et al., 2004) investigations have demonstrated that deviatoric stress should cause formation of melt-rich networks. Melt localization in partially molten rocks under shear stress would occur as a result of competition between two driving forces (Holtzman and Kohlstedt, 2007; Kohlstedt and Holtzman, 2009), namely shear stress gradient and surface tension. In the laboratory, melt migration is likely to be predominantly controlled by the shear stress gradient rather than surface tension. At low shear stresses, surface tension should be a significant driving force and contribute to melt redistribution toward an isotropic configuration to achieve the minimum interfacial energy in the system. However, the bulk contribution of surface tension to the melt distribution decreases with increasing grain size. Hence stress-induced melt migration can dominate over surface tension even at low stress conditions in the asthenosphere as well as at high stress conditions in the laboratory (Holtzman and Kohlstedt, 2007; Kohlstedt and Holtzman, 2009). It is worth noting that some geological evidence for stress-driven melt localization has been found in partially molten mantle rocks, for example, dunite in the Oman Ophiolite (Braun and Kelemen, 2002).

Stress-induced anisotropy is a common feature of physical properties in partially molten rocks, particularly of elasticity and viscosity (Takei, 2001). Cyclic loading tests have shown that elastic anisotropy induced by shear stress developed quickly via melt migration at the grain scale (Takei, 2010). However, this study demonstrates that the formation of conductivity anisotropy (~200 min after the onset of piston advancement) requires a considerably longer time scale than elastic response. This prolonged process suggests that the formation of well-connected melt channels parallel to shear direction requires more time than melt migration at the grain scale, indicating that the melt must be redistributed over considerably greater distances. The time required for the development of conductivity anisotropy was longer for runs with a relatively lower strain rate. The process that formed the melt channels depended on strain rate (or stress). On the other hand, the magnitude of conductivity anisotropy became constant for each deformation run independently of shear strain (Fig. 5). This suggests that once melt channel parallel to the shear direction was formed, conductivity varies little by further development of interconnection of the partial melt by the additional shear strain. Indeed, the post-experimental melt distributions of each run were remarkably similar to each other (Fig. 7) and were independent of melt composition and shear strain.

4.3. Geophysical implications

Several recent MT surveys have revealed strong electrical anisotropy at the top of the oceanic asthenosphere. Fig. 9 shows a comparison of laboratory-based conductivity-depth profiles with geophysical models underneath the Pacific Ocean. The conductivity largely increases with increasing depth from 50 km to 100 km near the East Pacific Rise (Evans et al., 2005; Baba et al., 2006). The conductivity values at this depth interval are higher than those determined from a semi-global model (Lizarralde et al., 1995) and the Philippines Sea (Baba et al., 2010). Conductivity anisotropy has been observed in such high-conductivity regions. At depths of approximately 100 km, the difference in conductivities between the directions parallel and normal to the plate motion ($10^{-0.6}$ to 10^{-1} S/m and $10^{-1.4}$ to 10^{-2} S/m, respectively) reaches one order of magnitude (Evans et al., 2005). The experimental results of this study suggest that such high anisotropy of conductivity in the direction of plate motion can be caused by strong alignment of partial melt parallel to shear direction.

Fig. 9 shows that the magnitude of anisotropy of the sheared partially molten peridotite agrees with those observed near the Eastern Pacific Rise (Evans et al., 2005; Baba et al., 2006), although this consistency does not necessarily mean that development of the high melt connectivity in the shear direction at the scale of a few millimeter observed in this study is applicable to that at

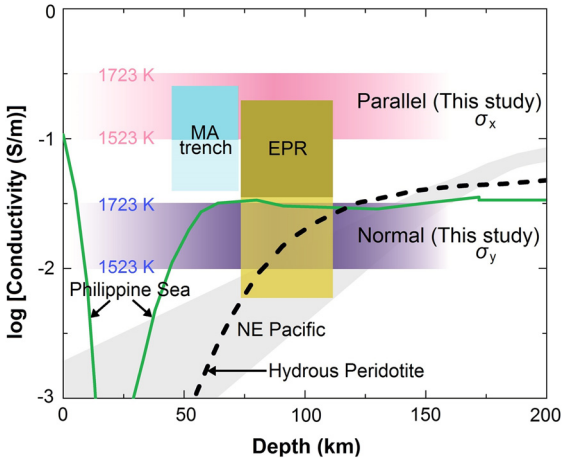

Fig. 9. Comparison of experimental conductivity data from this study with the geophysically observed electrical conductivity in the upper mantle beneath the oceanic plate. The purple and blue areas indicate the anisotropic conductivity values of partially molten peridotite obtained in this study. The dark yellow and yellow areas (EPR) indicate, respectively, the range of conductivities in directions parallel and normal to the plate motion near the East Pacific Rise (Evans et al., 2005). The cyan and light cyan areas (MA trench) indicate, respectively, the range of conductivities in directions parallel and normal to the plate motion beneath the edge of the Cocos plate at the Middle America trench offshore of Nicaragua (Naif et al., 2013). The light gray area denotes the geophysically observed conductivity profile beneath the northeastern Pacific (Lizarralde et al., 1995). The green line indicates the conductivity distribution beneath the Philippine Sea (Baba et al., 2010). The black dashed line represents the upper limit of conductivity of hydrous peridotite containing the maximum amount of water (Zhang et al., 2012). (For interpretation of the references to color in this figure legend, the reader is referred to the web version of this article.)

the scale of several tens of kilometers given by MT surveys at around depth of 100 km. 2 vol.% of basaltic melt used in this study is consistent with that predicted in low seismic-velocity regions beneath the Eastern Pacific Rise (Forsyth et al., 1998). However, temperature (∼1523 K) explaining the absolute conductivity value seems to be lower than solidus temperature of peridotite (1650 K) at the 100 km depth beneath the young ocean floor (Yoshino and Katsura, 2013). Since the absolute conductivity values of a partial molten rock also depend on melt fraction, degree of melting in this region slightly far from the mid-ocean ridge might be low.

On the other hand, the degree of the anisotropy in the Middle America trench offshore of Nicaragua (Naif et al., 2013) is only 0.4 log units, much smaller than that in the present study, whereas the absolute value is higher than that in the present study. The small magnitude of the anisotropy compared to the experimental results can be considered by difference of shear stress. Since electrical conductivity measurement under hydrostatic condition showed no evidence of the conductivity anisotropy, the magnitude of the anisotropy should gradually increase with decreasing shear stress. In this study, y-direction conductivity was held at constant value under shear stress, indicating that the connectivity of partial melt is no change. Assuming that the y-direction conductivity corresponds to the bulk conductivity under hydrostatic condition, the conductivity normal to the plate motion observed in the Middle America is not only much higher than that near the Eastern Pacific Rise, but also higher than that of basaltic melt. Thus the melt conductivity should be higher than that of dry basalt.

Laboratory measurements (Gaillard et al., 2008; Yoshino et al., 2010, 2012; Ni et al., 2011) showed that the volatile components of H_2O and CO_2 greatly increase melt conductivity. It is found that the electrical conductivity of melt-bearing peridotite will increase by more than one order when melt fraction increases from 0.01 to 0.1 (Yoshino et al., 2010). Likewise, if H_2O content increases from 0.02 to 4.1 wt.% in hydrous basaltic melt (Ni et al., 2011) or CO_2 concentration increases from 10 to 50 wt.% in partial molten carbonate peridotite (Yoshino et al., 2012), the melt conductivity would lead to 1.5 orders increase in conductivity. Recently Sifré et al. (2014) suggested that the incipient melts of carbonated peridotite are much higher than CO_2-free hydrated melts or hydrated minerals. Thus, one possible explanation for a high conductivity anomaly observed near the Middle America (Naif et al., 2013) is that this region has lower melt fraction but containing higher volatile contents.

The sharp seismic discontinuity observed at LAB invokes a horizontal sharp contrast of shear wave velocity between lithosphere and asthenosphere, and is not consistent with tube-like melt distribution. Although Caricchi et al. (2011) reported reduction of connectivity normal to the shear direction and denied the presence of horizontal melt-rich layers, the present results demonstrate that the y-direction conductivity during shear deformation kept a constant value, suggesting that the partial melt could maintain the interconnection along the shear plane. Thus, the shear plane would continue to behave as weak plane during shear deformation. The development of melt-rich channel parallel to the plate motion largely contributes to the conductivity anisotropy, while the horizontal connectivity of melt is probably maintained by collection of melt from the horizontal melt-depleted region. On the other hand, the z direction conductivity reduced to the olivine conductivity, suggesting the destruction of interconnection in the vertical direction. As a result, a horizontal layering composed of melt-rich and melt-depleted regions could be formed at LAB as proposed by Kawakatsu et al. (2009). The presence of such melt-rich shear planes could assist smooth sliding of rigid lithosphere plates on a mechanically weak asthenosphere.

The high conductivity anisotropy observed at the top of asthenosphere can be explained by high degree of melt connectivity in the spreading direction coupled with relatively lower connectivity in the ridge parallel direction. It seems to be consistent with some seismic observations showing a presence of low-velocity fingers oriented sub-parallel to the direction of absolute plate motion in the asthenosphere beneath the Pacific Ocean (e.g., Weeraratne et al., 2007; Harmon et al., 2011; French et al., 2013). The observed finger-like low-velocity pattern has been explained in the form of small-scale convection or viscous fingering instabilities. If the melt alignment parallel to the shear direction enhances by positive feedback under simple shear as discussed before, the melt redistribution at grain scale can expand to the geophysically observable scale. Therefore, geophysical heterogeneities normal to the ridge can be attributed to development of the melt-channel aligned with plate motion as a result of continuous motion of the oceanic lithosphere.

A counterargument to the interpretation of smooth plate motion being caused by partial melting is that the partial melt should rapidly become segregated from the host peridotite because of the high permeability of melt in peridotite and the large density difference between melt and mantle minerals (Karato, 2014). On the other hand, recent accurate density and viscosity measurements of basaltic melts by *in situ* X-ray analysis suggested that as melt ascends in the asthenosphere, melt can accumulate at depths of 80–100 km because of the diminishing mobility of magma (Sakamaki et al., 2013). However, the estimated accumulation depth is considerably deeper than that of the Gutenberg discontinuity (∼70 km) (Schmer, 2012). The present conductivity measurements can provide the other possible mechanism for magma retention at the LAB. The large increase in conductivity in the x direction, the lack of conductivity change in the y direction and the decrease in the z direction suggest that the interconnection of melt is broken in the direction normal to the shear plane. Takashima and Kurita (2008) found a power relationship (power exponent is 2) between permeability and electrical conductivity

based on permeability and electrical conductivity measurements. Thus, anisotropic melt distribution under shear stress can largely reduce upward permeability by several orders of magnitude, suggesting that the partial melt can be retained at the top of the asthenosphere. Thus, partial melt will allow smooth motion of the oceanic lithosphere over long periods. This idea is consistent with the seismic observations of the sharp LAB (Rychert et al., 2005; Kawakatsu et al., 2009; Schmer, 2012).

5. Conclusion

We performed conductivity measurement at 1 GPa simultaneously parallel and normal to the shear direction on the shear plane, and perpendicular to the shear plane in partially molten peridotite as functions of time and strain rate. It is found that electrical conductivity parallel to shear direction increases under shear stress and become constant, whereas that normal to the shear direction on the shear plane is constant. Conductivity difference between parallel and normal to shear direction finally reached one order of magnitude. The high anisotropy of conductivity in the direction of plate motion can be well explained by anisotropic interconnection of melt in partially molten rocks at the top of asthenosphere, but not hydration of nominally anhydrous minerals. Therefore, our results provide the direct experimental evidence for supporting these geophysically observed high-conductivity anisotropy at the LAB and verify the validity of partial melting hypothesis.

Acknowledgements

An anonymous reviewer and Fabrice Gaillard provided critical reviews that improved this paper. This work was supported by a Grant-in-Aids for Scientific Research Grant Number 24244087 to TY from the Japan Society for Promotion of Science, and partially supported by the Hundred Talent Program of CAS and NSFC (41303048) to BZ.

References

Baba, K., Chave, A.D., Evans, R.L., Hirth, G., Mackie, R.L., 2006. Mantle dynamics beneath the East Pacific Rise at 17°S: insights from the Mantle Electromagnetic and Tomography (MELT) experiment. J. Geophys. Res. 111, B02101. http://dx.doi.org/10.1029/2004JB003598.

Baba, K., Utada, H., Goto, T., Kasaya, T., Shimizu, H., Tada, N., 2010. Electrical conductivity imaging of the Philippine Sea upper mantle using seafloor magnetotelluric data. Phys. Earth Planet. Inter. 183, 44–62. http://dx.doi.org/10.1016/j.pepi.2010.09.010.

Braun, M., Kelemen, P., 2002. Dunite distribution in the Oman Ophiolite: implications for melt flux through porous dunite conduits. Geochem. Geophys. Geosyst. 3, 8603. http://dx.doi.org/10.1029/2001GC000289.

Caricchi, L., Gaillard, F., Mecklenburgh, J., Le Trong, E., 2011. Experimental determination of electrical conductivity during deformation of melt-bearing olivine aggregates: implications for electrical anisotropy in the oceanic low velocity zone. Earth Planet. Sci. Lett. 302, 81–94. http://dx.doi.org/10.1016/j.epsl.2010.11.041.

Constable, S., 2006. SEO3: a new model of electrical conductivity. Geophys. J. Int. 166, 435–437. http://dx.doi.org/10.1111/j.1365-246X.2006.03041.x.

Evans, R.L., Hirth, G., Baba, K., Forsyth, D., Chave, A., Mackie, R., 2005. Geophysical evidence from the MELT area for compositional controls on oceanic plates. Nature 437, 249–252. http://dx.doi.org/10.1038/nature04014.

Faul, U.H., Toomey, D.R., Waff, H.S., 1994. Intergranular basaltic melt is distributed in thin, elongated inclusions. Geophys. Res. Lett. 21, 29–32. http://dx.doi.org/10.1029/93GL03051.

Férot, A., Bolfan-Casanova, N., 2012. Water storage capacity in olivine and pyroxene to 14 GPa: implications for the water content of the Earth's upper mantle and nature of seismic discontinuities. Earth Planet. Sci. Lett. 349–350, 218–230. http://dx.doi.org/10.1016/j.epsl.2012.06.022.

Forsyth, D.W., et al., 1998. Imaging the deep seismic structure beneath a mid-ocean ridge: the MELT experiment. Science 280, 1215–1218. http://dx.doi.org/10.1126/science.280.5367.1215.

French, S., Lekic, V., Romanowicz, B., 2013. Waveform tomography reveals channeled flow at the base of the oceanic asthenosphere. Science 342, 227–230. http://dx.doi.org/10.1126/science.1241514.

Gaillard, F., Malki, M., Iacono-Marziano, G., Pichavant, M., Scaillet, B., 2008. Carbonatite melts and electrical conductivity in the asthenosphere. Science 322, 1363–1365. http://dx.doi.org/10.1126/science.1164446.

Harmon, N., Forsyth, D.W., Weeraratne, D.S., Yang, Y., Webb, S.C., 2011. Mantle heterogeneity and off axis volcanism on young Pacific lithosphere. Earth Planet. Sci. Lett. 311, 306–315. http://dx.doi.org/10.1016/j.epsl.2011.09.038.

Hashin, Z., Shtrikman, S., 1962. A variational approach to the theory of effective magnetic permeability of multiphase materials. J. Appl. Phys. 33, 3125–3131.

Hier-Majumder, S., Leo, P.H., Kohlstedt, D.L., 2004. On grain boundary wetting during deformation. Acta Mater. 52, 3425–3433. http://dx.doi.org/10.1016/j.actamat.2004.03.040.

Hirschmann, M.M., Tenner, T., Aubaud, C., Withers, A.C., 2009. Dehydration melting of nominally anhydrous mantle: the primacy of partitioning. Phys. Earth Planet. Inter. 176, 54–68. http://dx.doi.org/10.1016/j.pepi.2009.04.001.

Holtzman, B.K., Kohlstedt, D.L., Zimmerman, M.E., Heidelbach, F., Hiraga, T., Hustoft, J., 2003a. Melt segregation and strain partitioning: implications for seismic anisotropy and mantle flow. Science 301, 1227–1230. http://dx.doi.org/10.1126/science.1087132.

Holtzman, B.K., Groebner, N.J., Zimmerman, M.E., Ginsberg, S.B., Kohlstedt, D.L., 2003b. Stress-driven melt segregation in partially molten rocks. Geochem. Geophys. Geosyst. 4, 8607. http://dx.doi.org/10.1029/2001GC000258.

Holtzman, B.K., Kohlstedt, D.L., 2007. Stress-driven melt segregation and strain partitioning in partially molten rocks: effects of stress and strain. J. Petrol. 48, 2379–2406. http://dx.doi.org/10.1093/petrology/egm065.

Karato, S., 2014. Does partial melting explain geophysical anomalies? Phys. Earth Planet. Inter. 228, 300–306. http://dx.doi.org/10.1016/j.pepi.2013.08.006.

Kawakatsu, H., Kumar, P., Takei, Y., Shinohara, M., Kanazawa, T., Araki, E., Suyehiro, K., 2009. Seismic evidence for sharp lithosphere–asthenosphere boundaries of oceanic plates. Science 324, 499–502. http://dx.doi.org/10.1126/science.1169499.

Kohlstedt, D.L., Holtzman, B.K., 2009. Shearing melt out of the Earth: an experimentalist's perspective on the influence of deformation on melt extraction. Annu. Rev. Earth Planet. Sci. 37, 561–593. http://dx.doi.org/10.1146/annurev.earth.031208.100104.

Landauer, R., 1952. The electrical resistance of binary metallic mixtures. J. Appl. Phys. 23, 779–784.

Lizarralde, D., Chave, A.D., Hirth, G., Schultz, A., 1995. Northeastern Pacific mantle conductivity profile from long-period magnetotelluric sounding using Hawaii to California submarine cable data. J. Geophys. Res. 100, 17837–17854. http://dx.doi.org/10.1029/95JB01244.

McKenzie, D., Jackson, J.A., Priestley, K., 2005. Thermal structure of oceanic and continental lithosphere. Earth Planet. Sci. Lett. 233, 337–349. http://dx.doi.org/10.1016/j.epsl.2005.02.005.

Naif, S., Key, K., Constable, S., Evans, R.L., 2013. Melt-rich channel observed at the lithosphere–asthenosphere boundary. Nature 495, 356–359. http://dx.doi.org/10.1038/nature11939.

Ni, H., Keppler, H., Behrens, H., 2011. Electrical conductivity of hydrous basaltic melts: implications for partial melting in the upper mantle. Contrib. Mineral. Petrol. 162, 637–650. http://dx.doi.org/10.1007/s00410-011-0617-4.

Poe, B.T., Romano, C., Nestola, F., Smyth, J.R., 2010. Electrical conductivity anisotropy of dry and hydrous olivine at 8 GPa. Phys. Earth Planet. Inter. 181, 103–111. http://dx.doi.org/10.1016/j.pepi.2010.05.003.

Presnall, D.C., Simmons, C.L., Porath, H., 1972. Change in electrical conductivity of a synthetic basalt during melting. J. Geophys. Res. 77, 5665–5672.

Roberts, J.J., Tyburczy, J.A., 1999. Partial-melt electrical conductivity: influence of melt composition. J. Geophys. Res. 104, 7055–7065. http://dx.doi.org/10.1029/1998JB900111.

Rychert, C.A., Fischer, K.M., Rodenay, S., 2005. A sharp lithosphere–asthenosphere boundary imaged beneath eastern North America. Nature 434, 542–545. http://dx.doi.org/10.1038/nature03904.

Sakamaki, T., Suzuki, A., Ohtani, E., Terasaki, H., Urakawa, S., Katayama, Y., Funakoshi, K., Wang, Y., Hernlund, J.W., Ballmer, M.D., 2013. Ponded melt at the boundary between the lithosphere and asthenosphere. Nat. Geosci. 6, 1041–1044. http://dx.doi.org/10.1038/NGEO1982.

Schmer, N., 2012. The Gutenberg discontinuity: melt at the lithosphere–asthenosphere boundary. Science 335, 1480–1483. http://dx.doi.org/10.1126/science.1215433.

Shankland, T.J., Duba, A.G., 1990. Standard electrical conductivity of isotropic, homogeneous olivine in the temperature range 1200–1500 °C. Geophys. J. Int. 103, 25–31. http://dx.doi.org/10.1111/j.1365-246X.1990.tb01749.x.

Sifré, D., Gardes, E., Massuyeau, M., Hashim, L., Hier-Majumder, S., Gaillard, F., 2014. Electrical conductivity during incipient melting in the oceanic low-velocity zone. Nature 509, 81–85. http://dx.doi.org/10.1038/nature13245.

Soustelle, V., Walte, N.P., Manthilake, G., Frost, D.J., 2014. Melt migration and melt-rock reactions in the deforming Earth's upper mantle: experiments at high pressure and temperature. Geology 42, 83–86. http://dx.doi.org/10.1130/G34889.1.

Takashima, S., Kurita, K., 2008. Permeability of granular aggregate of soft gel: application to the partial molten system. Earth Planet. Sci. Lett. 267, 83–92. http://dx.doi.org/10.1016/j.epsl.2007.11.041.

Takei, Y., 2001. Stress-induced anisotropy of partially molten media inferred from experimental deformation of a simple binary system under acoustic monitoring. J. Geophys. Res. 106, 567–588. http://dx.doi.org/10.1029/2000JB900361.

Takei, Y., 2010. Stress-induced anisotropy of partial molten rock analogue deformed under quasi-hydrostatic loading test. J. Geophys. Res. 115, B03204. http://dx.doi.org/10.1029/2009JB006568.

ten Grotenhuis, S.M., Drury, M.R., Spiers, C.J., Peach, C.J., 2005. Melt distribution in olivine rocks based on electrical conductivity measurements. J. Geophys. Res. 110, B12201. http://dx.doi.org/10.1029/2004JB003462.

Toramaru, A., Fujii, N., 1986. Connectivity of melt phase in a partially molten peridotite. J. Geophys. Res. 91, 9239–9252. http://dx.doi.org/10.1029/JB091iB09p09239.

Waff, H.S., Bulau, J.R., 1979. Equilibrium fluid distribution in an ultramafic partial melt under hydrostatic conditions. J. Geophys. Res. 84, 6109–6114.

Weeraratne, D.S., Forsyth, D.W., Yang, Y.J., Webb, S.C., 2007. Rayleigh wave tomography beneath intraplate volcanic ridges in the South Pacific. J. Geophys. Res. 112, B06303. http://dx.doi.org/10.1029/2006JB004403.

Xu, Y., Shankland, T.J., Poe, B.T., 2000. Laboratory-based electrical conductivity in the Earth's mantle. J. Geophys. Res. 105, 27865–27875. http://dx.doi.org/10.1029/2000JB900299.

Yang, X.Z., 2012. Orientation-related electrical conductivity of hydrous olivine, clinopyroxene and plagioclase and implications for the structure of the lower continental crust and uppermost mantle. Earth Planet. Sci. Lett. 317–318, 241–250. http://dx.doi.org/10.1016/j.epsl.2011.11.011.

Yoshino, T., Takei, Y., Wark, D.A., Watson, E.B., 2005. Grain boundary wetness of texturally equilibrated rocks, with implications for seismic properties of the upper mantle. J. Geophys. Res. 110, B08205. http://dx.doi.org/10.1029/2004JB003544.

Yoshino, T., Matsuzaki, T., Yamashita, S., Katsura, T., 2006. Hydrous olivine unable to account for conductivity anomaly at the top of the asthenosphere. Nature 443, 973–976. http://dx.doi.org/10.1038/nature05223.

Yoshino, T., Yamazaki, D., Mibe, K., 2009. Well-wetted olivine grain boundaries in partial molten peridotite in the asthenosphere. Earth Planet. Sci. Lett. 283, 167–173. http://dx.doi.org/10.1016/j.epsl.2009.04.007.

Yoshino, T., Laumonier, M., Mclsaac, E., Katsura, T., 2010. Electrical conductivity of basaltic and carbonatite melt-bearing peridotites at high pressures: implications for melt distribution and melt fraction in the upper mantle. Earth Planet. Sci. Lett. 295, 593–602. http://dx.doi.org/10.1016/j.epsl.2010.04.050.

Yoshino, T., Mclsaac, E., Laumonier, M., Katsura, T., 2012. Electrical conductivity of partial molten carbonatite peridotite. Phys. Earth Planet. Inter. 194–195, 1–9. http://dx.doi.org/10.1016/j.pepi.2012.01.005.

Yoshino, T., Katsura, T., 2013. Electrical conductivity of mantle minerals: role of water in conductivity anomalies. Annu. Rev. Earth Planet. Sci. 41, 605–628. http://dx.doi.org/10.1146/annurev-earth-050212-124022.

Zhang, B.H., Yoshino, T., Wu, X.P., Matsuzaki, T., Shan, S.M., Katsura, T., 2012. Electrical conductivity of enstatite as a function of water content: implications for the electrical structure in the upper mantle. Earth Planet. Sci. Lett. 357–358, 11–20. http://dx.doi.org/10.1016/j.epsl.2012.09.020.